Tribology International 174 (2022) 107771

Contents lists available at ScienceDirect

Tribology International

journal homepage: www.elsevier.com/locate/triboint

Behavior of the hard phases of copper alloys subjected to cavitation erosion investigated by SEM observation

Ye Tian [a,b], Hang Zhao [a,b], Rui Yang [a,b], Haijun Zhang [a,b], Miao Yu [a,b], Ping Zhou [a,b], Hua Li [a,b,c], Xiuyong Chen [a,b,c,*]

[a] Key Laboratory of Marine Materials and Related Technologies, Zhejiang Key Laboratory of Marine Materials and Protective Technologies, Ningbo Institute of Materials Technology and Engineering, Chinese Academy of Sciences, Ningbo 315201, China
[b] Zhejiang Engineering Research Center for Biomedical Materials, Cixi Institute of Biomedical Engineering, Ningbo Institute of Materials Technology and Engineering, Chinese Academy of Sciences, Ningbo 315201, China
[c] School of Engineering Science, University of Chinese Academy of Sciences, Beijing 100049, China

ARTICLE INFO

Keywords:
Copper alloys
Cavitation erosion
Microstructure evolution
Scanning electron microscopy

ABSTRACT

This work investigated the cavitation erosion performance of two copper alloys in deionized water (DW) and artificial seawater (ASW) for 10 h. Specifically, scanning electron microscopy observation was performed on the alloys exposed to cavitation erosion for different periods (within 3 h) at the same sites to study the microstructural evolution. The results tested in DW showed that the accumulation of the stress at phase boundaries caused crack generation in the α phase and severe deformation of the hard phases (κ & Fe(Al,Cu)), resulting in the exfoliation of the hard phases. However, the deformation of the hard phase was not observed from the samples tested in ASW due to stress corrosion cracking and material dissolution at the phase boundaries.

1. Introduction

Cavitation erosion is a type of wear that frequently occurs to the components operating in a fluid [1,2]. Generally, cavitation refers to the rupture of a fluid caused by a local pressure reduction below saturation vapor pressure level, resulting in generation of cavitation bubbles [3]. However, cavitation bubbles are unstable and can easily collapse, causing the release of shock waves/microjets. As a result, the components will suffer from severe erosion by the repeated impacts of the shock waves/microjets and it can eventually come to failure [4]. Copper alloys, such as nickel aluminum bronze (NAB) and aluminum bronze (AB), exhibit good mechanical properties and resistance to wear and corrosion [5]. Thus, they are commonly used to manufacture the components such as turbines, propellers, and valves, which are frequently exposed to cavitation erosion [6].

The urgent need for the copper alloys with high resistance to cavitation erosion has encouraged many studies on the failure mechanism of the copper alloys subjected to cavitation erosion [7–9]. Many studies indicated that the different phases of the copper alloys showed different responses to cavitation erosion, and cracks tended to initiate at phase boundaries [10–12]. Qin et al. [13] found that heat treatment could increase the hard phase content in NAB, thereby improving the cavitation erosion resistance of NAB. Specifically, the cavitation erosion rate of the quenched-aged sample was 87.34% lower than that of the original sample. Zhang et al. [14] discovered that the synergistic effect between cavitation erosion and corrosion in NaCl solution accounted for 41.44% of the total mass loss, demonstrating the critical impact of the synergy on the cavitation erosion of NAB. Meanwhile, the accelerated erosion rate was closely related to the accelerated crack propagation due to corrosion. Basumatary et al. [15] demonstrated that cracks could be observed under the surface up to a depth of 150 μm after 5 h of cavitation erosion in NaCl solution. The research also showed that the α phase around κ phases could be preferentially eroded, which would lead to the exposure of the κ phases and the formation of cavitation craters. According to the effects of microstructures on cavitation erosion behavior, many methods have been developed to improve the cavitation erosion resistance of copper alloys, such as friction stir processing, laser surface treatment, heat treatment, and ultrasonic surface rolling process [13,16–19]. However, the failure mechanism of the copper alloys exposed to cavitation erosion is not thoroughly understood, which limits the design of

* Corresponding author at: Key Laboratory of Marine Materials and Related Technologies, Zhejiang Key Laboratory of Marine Materials and Protective Technologies, Ningbo Institute of Materials Technology and Engineering, Chinese Academy of Sciences, Ningbo 315201, China.
E-mail address: chenxiuyong@nimte.ac.cn (X. Chen).

https://doi.org/10.1016/j.triboint.2022.107771
Received 5 May 2022; Received in revised form 28 June 2022; Accepted 5 July 2022
Available online 8 July 2022
0301-679X/© 2022 Elsevier Ltd. All rights reserved.

the copper alloys with further enhanced resistance to cavitation erosion.

At present, the study of the cavitation erosion behavior of materials is based on a few techniques, including mass loss, scanning electron microscopy (SEM), transmission electron microscope (TEM), electron backscatter diffraction (EBSD), and electrochemical analysis [15,20–24]. Although the microstructural evolution process of samples subjected to cavitation erosion can be inferred from the above methods, the derived microstructural evolution process may not be accurate because it was based on the results from different positions on eroded surfaces. We recently adopted an SEM analysis that observed the same position of the eroded sample to explore the failure mechanisms of austenitic stainless steels subjected to cavitation erosion, presenting pre-existing pores were not the starting point of the failure in austenitic stainless steels [25]. In addition, other work also suggested that the SEM observation at the same position greatly assisted in investigating the cavitation erosion failure mechanism of many materials [3,26,27]. Nevertheless, the research on the cavitation erosion performance of the copper alloys based on SEM observation at the same position is still absent.

In this study, the cavitation erosion behavior of NAB and AB in deionized water (DW) and artificial seawater (ASW) was observed. The cumulative volume loss and the rate of volume loss of the NAB and AB exposed to cavitation erosion in both media were measured. Furthermore, the microstructure evolution of the NAB and AB during cavitation erosion in both media was studied by SEM observation, which could be used to guide the design of copper alloys with good cavitation erosion resistance.

2. Experimental

2.1. Materials and sample preparation

Both NAB and AB used in this study are commercially available (Suzhou Zhongmai Copper Co., Ltd., Jiangsu, China). The samples used in this study were cylindrical with a diameter of 20 mm and a thickness of 10 mm. The chemical composition of the samples is listed in Table 1. All the samples were ground to 2000-grit sandpaper, polished with 2.5 μm diamond suspension, and finished with 0.05 μm colloid silica, respectively. The polished samples were ultrasonic cleaned in deionized water, then in ethanol for 10 mins, and finally were dried in a vacuum at 25 ℃.

The polished samples were etched for 3 s in the etchant containing $FeCl_3$ (5 g), HCl (37 wt%, 2 ml), and 95 ml ethanol [28]. After etching, these samples were flushed by DW. Then, they were rinsed in ethanol and followed by ultrasonic cleaning in ethanol for 5 mins. Finally, the samples were dried in a vacuum at 25 ℃. These etched samples were observed by scanning electron microscope (SEM, Regulus 8230, Hitachi Ltd, Tokyo, Japan) to identify the phases in the samples.

2.2. Cavitation erosion tests

Cavitation erosion tests were carried out using ultrasonic vibratory apparatus (GBS-SCT 20 A, Hangzhou Guobiao Ultrasonic Equipment Co., Ltd., China) as per a modified version of ASTM G32 [29] resonating at 20 kHz with a peak-to-peak amplitude of 50 μm. A detailed schematic diagram of this setup can be found in a previous study [30]. The test media were ASW (as per ASTM D1141–98 [31]) and DW, whose temperature was kept at 25 ± 2 ℃ during the test. The ultrasonic horn tip was submerged 23 ± 2 mm beneath the liquid level of the test medium, and the sample was placed at a standoff distance of 1 mm from the horn tip [30]. The cavitation erosion test lasted for 10 h for each sample, and the sample was weighed by a balance with a scale division of 0.1 mg at every interval of 1 h, giving the cumulative mass loss. Average cumulative mass loss was calculated based on 3 samples. Then, the average cumulative volume loss was figured out by the mass loss and the density of the NAB and AB, which are 7.8 g/cm^3 and 7.6 g/cm^3, respectively. In addition, the samples exposed to cavitation erosion for 10 h were observed in SEM.

Table 1
Chemical composition of NAB and AB.

Samples	Al (wt %)	Fe (wt %)	Ni (wt %)	Mn (wt %)	Si (wt %)	C (wt %)	Cu (wt%)
NAB	9.24	4.56	4.73	1.31	0.12	0.06	balance
AB	10.23	4.19	0.03	0.15	0.05	0.03	balance

2.3. SEM characterization for failure mechanism

The same regions on the samples before and after certain test intervals were observed by SEM, showing the microstructure evolution of the NAB and AB samples exposed to cavitation erosion and revealing the failure mechanism. The original polished samples for the SEM observation were slightly etched to expose the phase boundaries before cavitation erosion test.

3. Results and discussion

3.1. Microstructure characterization

Fig. 1 shows the microstructure of the NAB and AB after etching. The microstructure of the NAB consisted of fcc copper-rich α matrix (Fig. 1**a**), martensitic bcc β' phases (or retain β phases) (Fig. 1**a**), and κ phases. The κ phases are coordination compounds of Ni-Fe-Al and are sorted into κ_I, κ_{II}, κ_{III}, and κ_{IV} according to their phase composition, morphology, and distribution (Fig. 1**b**) [32,33]. Specifically, the κ_I phase showed a large rosette-shaped morphology. The κ_{II} phase was a spherical particle with a typical size of 0.5–1 μm, which was generally found at the boundaries of the α and β′ phases. The κ_{III} phase shows a typical lamellar eutectoid morphology, and the κ_{IV} phase manifests as nano-scale spherical precipitates. For AB, α matrix, β phases, κ phases, and Fe (Al, Cu) phases were observed (Fig. 1c and Fig. 1**d**). The microstructure of NAB and AB observed in this study is identical to the reported literature [11,34,35].

3.2. Volume loss during cavitation erosion

The cavitation erosion resistance of NAB and AB in DW and ASW was represented by the plots of cumulative volume loss and volume loss rate versus cavitation erosion time (Fig. 2). The cumulative volume loss of all the samples increased as the exposure to cavitation erosion was extended (Fig. 2**a**). Meanwhile, the cumulative volume loss in ASW was much higher than the sample tested in DW, suggesting that the ASW may accelerate material loss during cavitation erosion. This result was consistent with the previously reported studies [22,36–38]. It is worth noticing that the samples tested in ASW exhibited a sudden increase in the volume loss rate at the initial stage (the first hour) of cavitation erosion (Fig. 2**b**). The suddenly increased volume loss rate could attribute to the removal of exposed hard residual phases (caused by surface finishing during sample preparation) at the initial stage of cavitation erosion, as these residual phases may be weakly bonded to the matrix. Apart from the sudden increase in the volume loss rate in the first hour of cavitation erosion, all the samples exhibited a typical erosion rate versus time curve, clearly presenting incubation, acceleration, and maximum rate (or steady-state) periods [39]. As shown in Fig. 2**b**, the samples tested in ASW exited the incubation period after 2 h, while the samples tested in DW had a longer incubation period (5 h for NAB and 4 h for AB). After the acceleration period, the samples tested in ASW and DW entered the steady period at the 6th and 7th hours, respectively. Despite the similar plots in Fig. 2, AB exhibited more volume losses and showed a greater erosion rate than NAB, either in ASW or DW. Furthermore, the result in Fig. 2**b** also suggested that the ASW shortened the incubation

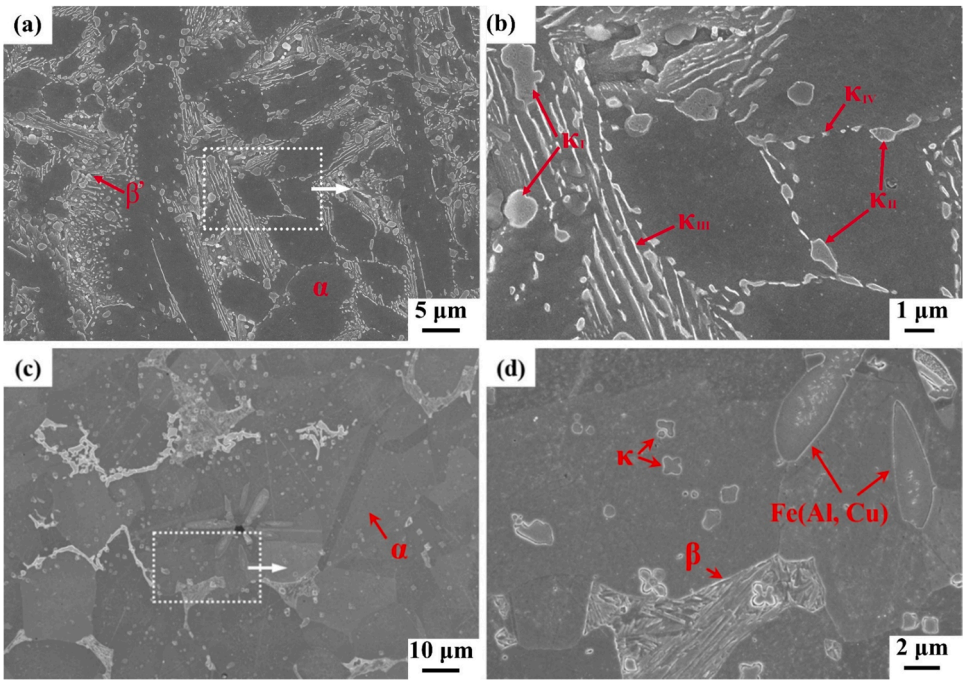

Fig. 1. The SEM images of (a, b) NAB and (c, d) AB.

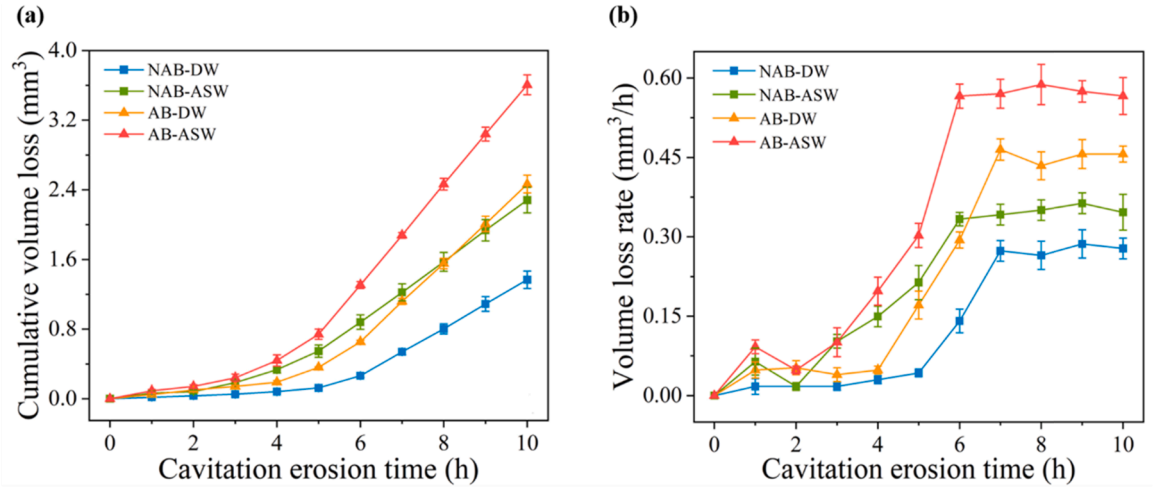

Fig. 2. The cumulative volume loss (a) and volume loss rate (b) versus cavitation time for the NAB and AB exposed to cavitation erosion in DW and ASW solutions.

period and brought forward the steady period, indicating a possible synergistic effect of cavitation erosion-corrosion in ASW, which may accelerate material damage [14].

3.3. Surface morphology after cavitation erosion

The damaged surface of the samples after cavitation erosion in DW and ASW solutions for 10 h are shown in Fig. 3. Craters and cracks formed on the samples after cavitation erosion in both media, resulting in roughened and damaged surfaces (Fig. 3 **a1-d1**). The magnified SEM image in Fig. 3 **a2** shows fatigue striations of the NAB tested in DW, which are also commonly observed in other materials subjected to cavitation erosion [40]. Cracks were also seen in Fig. 3 **a2**. In contrast, fatigue striation was not observed from the NAB tested in ASW (Fig. 3 **b2**). Meanwhile, for the NAB tested in ASW, the cracks generated in the crater or nearby crater were shorter and more than that of the NAB in DW (Fig. 3 **a2** & **b2**), inferring that cracks were more easily formed in ASW. The rapid connection of cracks separated the material into small pieces, accelerating material spalling and leaving a roughened surface. Thus, the NAB exposed to cavitation erosion in ASW exhibited a rough surface and almost no fatigue striations (Fig. 3 **b2**). For AB, the results were similar. Cracks and craters were observed in the AB either tested in ASW or DW (Fig. 3**c-d**), while fatigue striations only appeared on the sample tested in DW (Fig. 3**c2**). The above results show that the failure mechanisms of the samples under cavitation erosion and cavitation erosion-corrosion conditions were completely different, which could be attributed to the synergistic effect of corrosion and cavitation erosion [41].

3.4. Microstructure evolution of the hard phases during cavitation erosion

Hard phases (including $\kappa_{I\text{-}IV}$ phases and Fe(Al, Cu) phase) can provide dispersion strengthening to copper alloys and also play an essential role in the cavitation erosion performance of copper alloys [13,35].

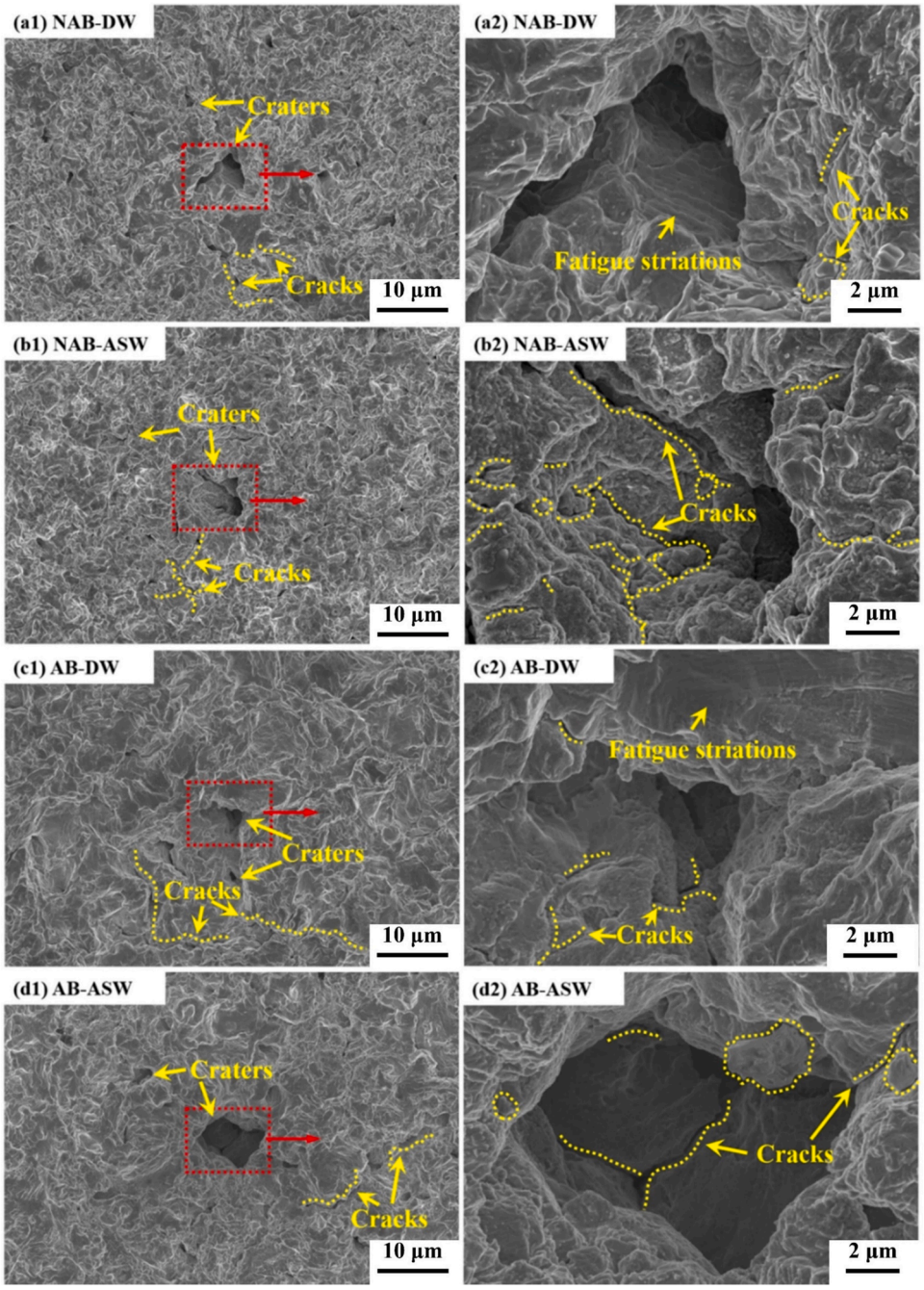

Fig. 3. Surface morphology of NAB and AB after cavitation erosion for 10 h in DW and ASW: (a1, a2) NAB in DW solution, (b1, b2) NAB in ASW solution, (c1, c2) AB in DW solution, and (d1, d2) AB in ASW solution.

Observing the evolution of the hard phases and the surrounding α phase of copper alloys during cavitation erosion process could provide a better understanding of the cavitation erosion failure mechanism of copper alloys. Fig. 4 shows the spalling process of the κ phase in NAB. Grain boundary (highlighted by the red dotted lines in Fig. 4**b**) sliding occurred after cavitation erosion for 40 mins. Meanwhile, the grains near the boundary (highlighted by the green dotted line) were pressed, and the cracks (highlighted by the yellow line) formed near the κ phase. As exposed to cavitation erosion further, the grain boundary continued slipping to the right. The grain near the grain boundary was gradually squeezed and spalled off (Fig. 4**d**). Meantime, the cracks extended around the κ phase. After cavitation erosion for 140 mins, the κ phase spalled off (Fig. 4**f**), forming a crater with a rough surface.

For the NAB in ASW solution, however, cracks formed after cavitation erosion for only 20 mins (indicated by the yellow dotted lines in Fig. 5**b**), and the number of the cracks that appeared in NAB after cavitation erosion in ASW is more than in DW. Meanwhile, most of the cracks were located around the α/κ phase boundaries. After cavitation erosion for 40 mins, the κ phases, including κ_I, κ_{II}, and κ_{III}, spalled off, forming a crater with a smooth surface (Fig. 5**c**). Moreover, the cracks propagated along the α grain boundaries or around the κ phases. Then, the κ phases were surrounded by cracks. As the cavitation erosion time increased (Fig. 5**d**-5**f**), more materials (mainly the κ phases) spalled off, and more craters were generated (highlighted by green dotted boxes). In addition, compared with the NAB tested in DW, cracks tended to develop around the κ phase in ASW and were wider.

AB and NAB are inevitably affected by the inner stress generated during casting when manufactured as a propeller used in the marine

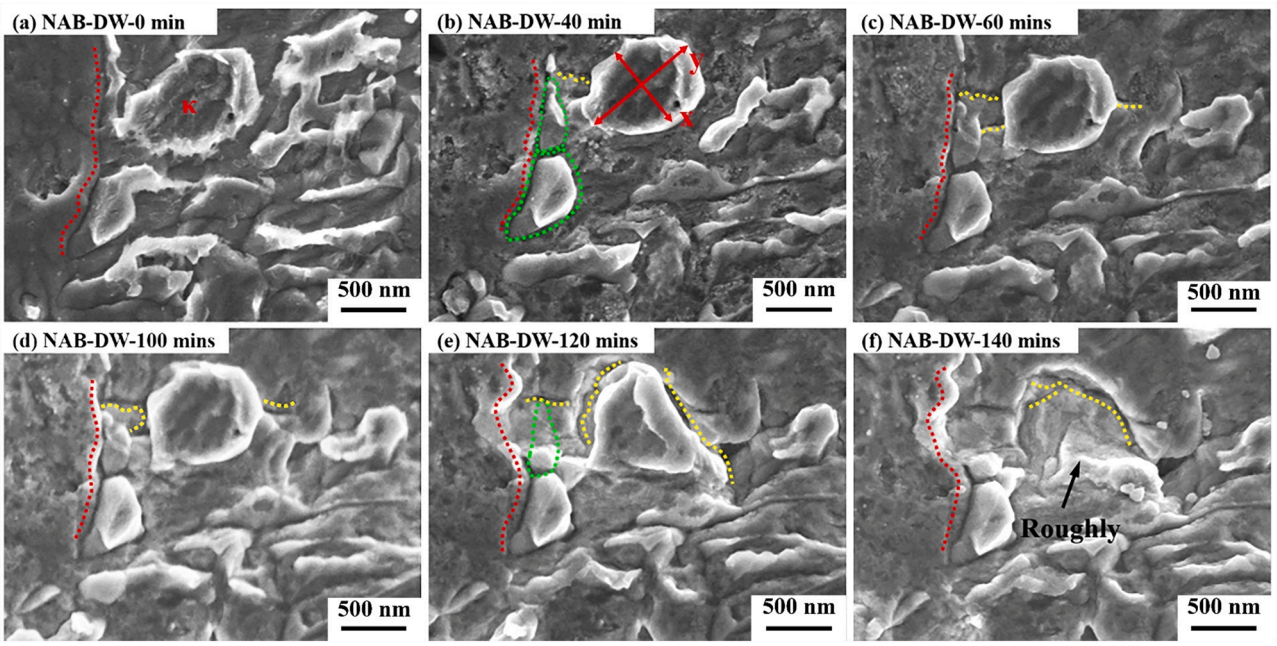

Fig. 4. The microstructural evolution of the NAB at the α/κ interface during cavitation erosion in DW for (a) 0 min, (b) 40 mins, (c) 60 mins, (d) 100 mins, (e) 120 mins, and (f) 140 mins. The grain boundary is highlighted by the red dotted line, the yellow dotted line highlights the crack, and the crater formed by the spalling of material is highlighted by the green dotted box.

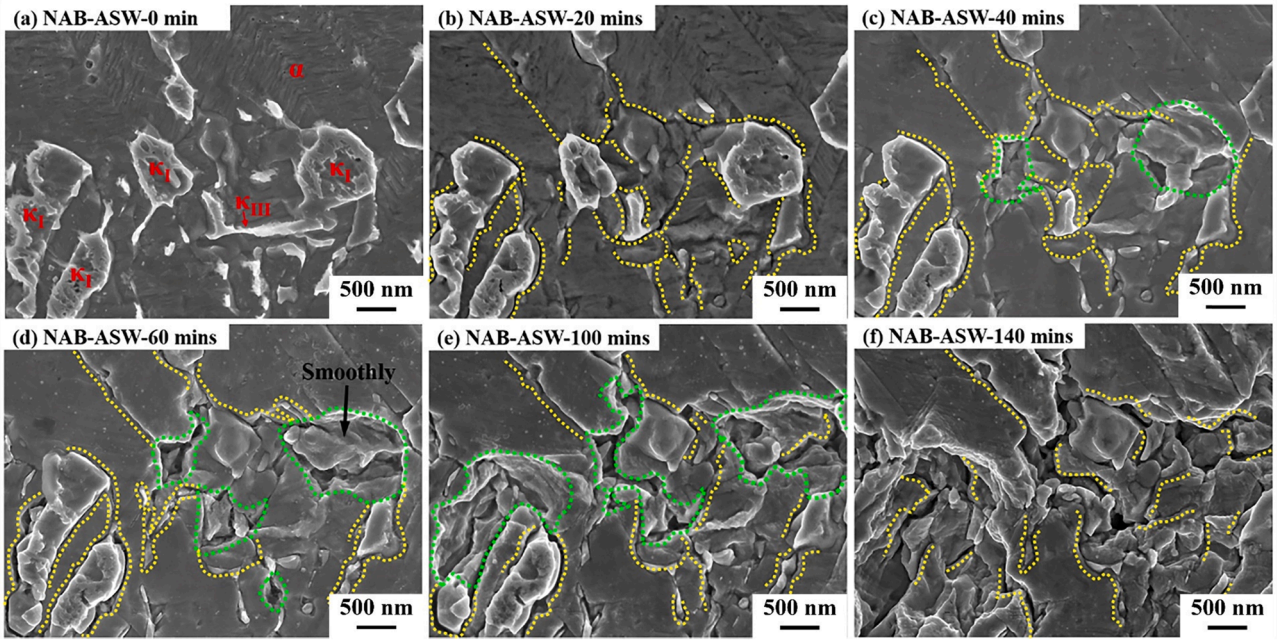

Fig. 5. The microstructural evolution of the NAB at α/κ interface during cavitation erosion in ASW for (a) 0 min, (b) 20 mins, (c) 40 mins, (d) 60 mins, (e) 100 mins, and (f) 140 mins. The yellow dotted line highlights the crack, and the crater formed by the spalling of material is highlighted by the green dotted box.

environment [42,43]. Meanwhile, collapse of cavitation bubbles also repeatedly impacts the material surface via stress pulses. These stress pulses can be up to GPa [44] and can cause stress accumulation in the material, which plays a vital role in the formation and propagation of cracks [45,46]. Obviously, the grain boundary sliding that occurred in the NAB during cavitation erosion in DW suggested glide and piling up of dislocations taking place in the interior of grains [47]. In addition, the κ phase can block dislocation movement and lead to stress accumulated near the κ phase, so the cracks formed around the κ phase [48]. The impact of high-speed micro-jet caused cracks to propagate along the κ phase boundary, resulting in the κ phase failure (Fig. 5**c**-5**f**). Conversely, no apparent phase boundary sliding was observed from the NAB surface after cavitation erosion in ASW. Meanwhile, most cracks were in the α phase around the κ phases, developed after cavitation erosion for 20 mins (Fig. 5**b**). This suggests the cracks could easily formed around the κ phases under the coupling effect of the corrosion attack and cavitation impact. Literature reported that the threshold stress level resulting in the stress corrosion cracking is below the yield strength in the nitrite solution [49], indicating the stress corrosion cracking easily formed under the coupling effect of applied stress and corrosive

medium. Stress corrosion cracking tends to form in the case of the low stress below the yield strength, and in this case, no slipping is generated by plastic deformation. Similar results were obtained in this study, which showed the phase boundary sliding was not observed from the NAB exposed to cavitation erosion in ASW, possibly attributed to the low threshold of stress corrosion cracking in ASW. Under the impact of microjets/shockwaves, the cracks formed at low-stress level, which could be up at short exposure to cavitation erosion. Therefore, more cracks were observed from the surface of the NAB in ASW than in DW. As shown in Fig. 5**d**, wide cracks formed around the κ phase (highlighted by the yellow dotted line) and a smooth interface formed, which may be caused by chemical dissolution of the α matrix in ASW [50].

Fig. 6 displays the microstructure evolution of the AB after cavitation erosion in DW. Cracks formed at the α/Fe(Al, Cu) interface (indicated by the yellow dotted line in Fig. 6**b**), and deformation (highlighted by the red arrows) was also observed. The deformation was aggravated with increased cavitation erosion time (Fig. 6**c**). When the time was up to 120 mins, the α matrix near the α/Fe(Al, Cu) interface spalled off, resulting in the formation of craters (highlighted by green dotted boxes in Fig. 6**d**). The cracks and the craters expanded along with prolonged time. The remained α matrix in the Fe(Al, Cu) phase was observed (Fig. 6**f**). However, no apparent grain boundary sliding was observed from the AB in ASW (Fig. 7). During the cavitation erosion in ASW, cracks and craters formed more easily (indicated by the yellow dotted lines and the green dotted boxes in Fig. 7). Meanwhile, the crater surfaces are smooth, and the α matrix was utterly detached from the Fe(Al, Cu) phase. The results above were in line with what was illustrated in Fig. 5. These results further evidenced that crack initiation can be more accessible in ASW than in DW. Therefore, the material damage usually preferentially occurred at the phase boundary in ASW.

Fig. 8 shows the microstructure evolution of the κ phase during cavitation erosion process in DW. It is worth noticing that the α matrix at the grain boundary (or twin boundary) of the α matrix was firstly damaged (highlighted by the green dotted box in Fig. 8**d**), while the κ phase was not (the white dotted boxes). With the increase of cavitation erosion time, the α matrix around the κ phase gradually spalled off (Fig. 8**e**). Finally, the κ phase was removed from the material, and once the κ phase was eroded, the α matrix was quickly worn (Fig. 8**f**). It shows that the α matrix was more easily damaged than the hard phases. However, the phase boundary at the α/κ interfaces gradually dissolved during cavitation erosion in ASW (Fig. 9**b & c**), resulting in the exposure of the κ phase. Subsequently, the α matrix continued to be dissolved and impacted (Fig. 9**d & e**). As a result, the α phase was severely damaged (Fig. 9**d & e**). After more exposure to cavitation erosion, the κ phase was removed from the α phase, resulting in the formation of a crater. This study showed that the corrosive ASW preferentially attacked at the phase boundary, in agreement with the literature [11].

According to Figs. 4, 6, and 8, the hard phases (κ phases and Fe(Al, Cu) phase) could undergo plastic deformation despite their relatively high hardness. The deformation index (D_i) is used to investigate the severity of the deformation, which is defined by the quotient of the aspect ratio of the hard phase after cavitation erosion divided by its original aspect ratio, and the result is shown in Fig. 10. It should be noted that the data in Fig. 10 were based on the observation of the hard phases in Figs. 4 and 8. According to Fig. 10, the D_i values of the samples decreased obviously with the cavitation erosion time increasing when the samples were tested in DW. The deformation degree of the κ phase is inversely proportional to the D_i value, which illustrates that the deformation degree of the κ phase increases with the test time. Generally, deformation is positively correlated to accumulated stress [51,52]. Interestingly, similar phenomena were not observed for the samples during the cavitation erosion test in ASW solution. With the increase of test time in ASW solution, the D_i values first increased slightly and then remained relatively stable. Specifically, the D_i value observed in Fig. 5 increased slightly from 1 (0 min) to 1.16 (40 mins), and then kept relatively stable during the subsequent cavitation erosion process. At the early stage of cavitation erosion in ASW solution, the dissolution of the α-κ phase boundary led to the gradual exposure of the κ phase [53], so the D_i values of the samples increased slightly. As the cavitation erosion continued, the D_i value remained relatively stable, indicating that no additional stress was exerted on the κ phase during the subsequent cavitation erosion process. Similar results were also observed from the Fe(Al, Cu) phase during the cavitation erosion process in DW (Fig. 6) and ASW solutions (Fig. 7). In DW solution, the Fe(Al, Cu) phase deformed seriously with the prolongation of cavitation erosion time (Fig. 6), but deformation was not observed in ASW solution (Fig. 7).

The α phase of the copper alloys has a typical fcc lattice structure and its hardness is lower than the hard phases (including the κ and the Fe(Al, Cu) phases) [54]. In general, the α phase has lower strain rate sensitivity and higher plastic deformation ability than the hard phases [14], which

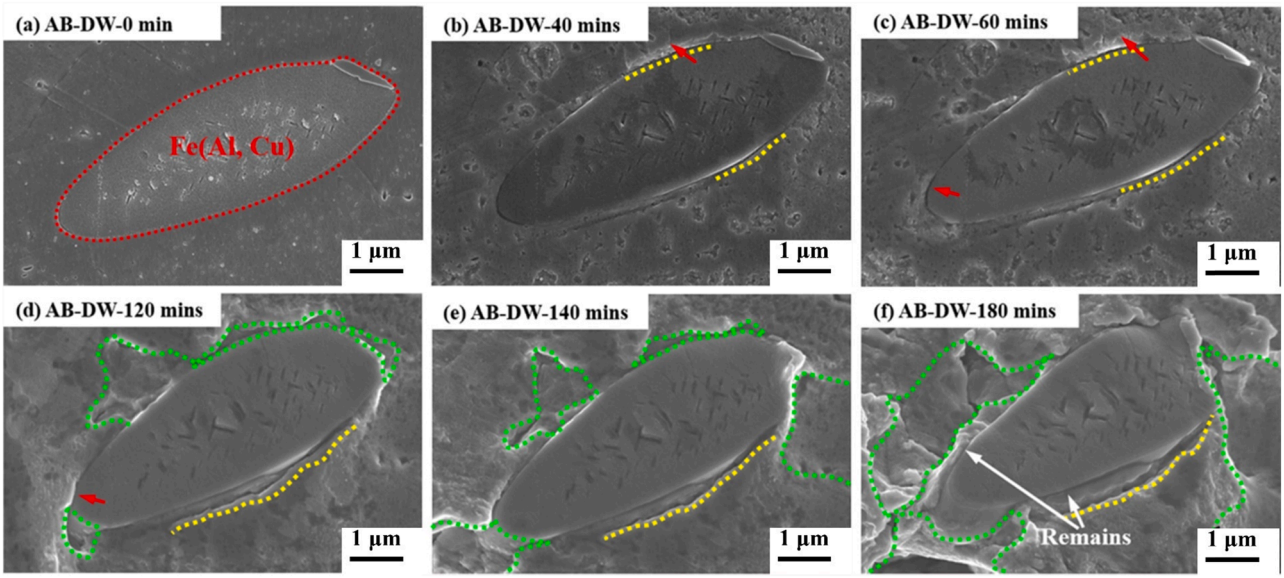

Fig. 6. The microstructural evolution of the AB at the α/Fe(Al, Cu) interface during cavitation erosion process in DW solution for (a) 0 min, (b) 40 mins, (c) 60 mins, (d) 120 mins, (e) 140 mins, and (f) 180 mins. The crack is highlighted by the yellow dotted line, and the crater formed by the spalling of material is highlighted by the green dotted box. The red arrow points out the deformation position. Fe(Al,Cu) phase is highlighted by the red dotted box.

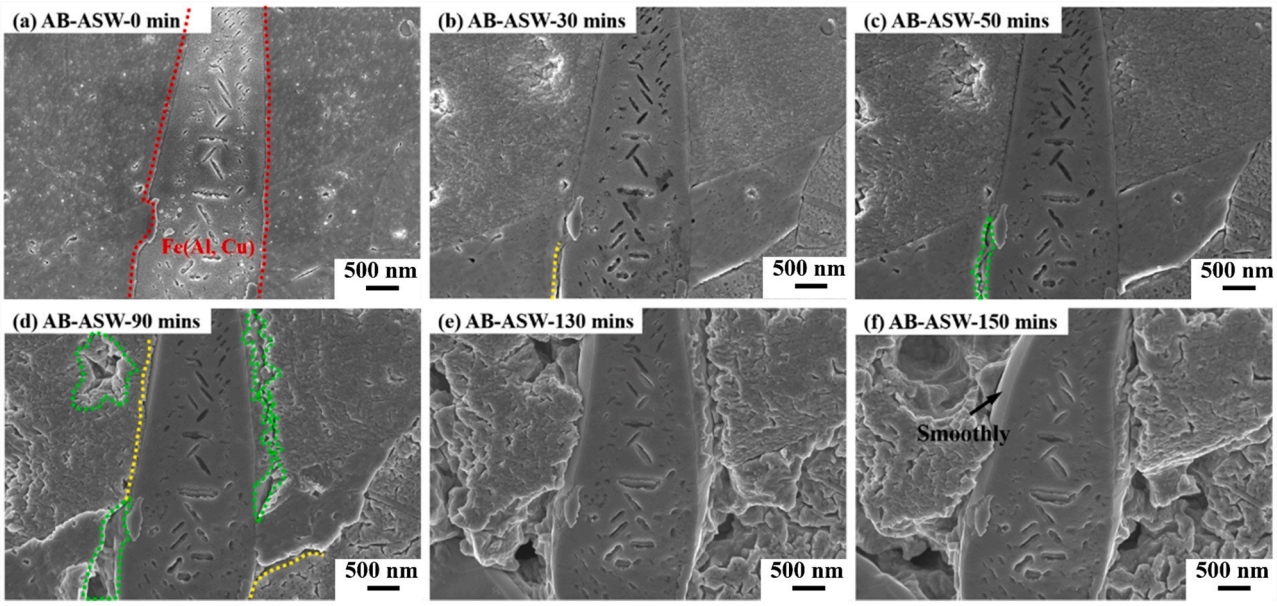

Fig. 7. The microstructural evolution of the AB at the α/Fe(Al, Cu) interface during cavitation erosion process in ASW solution for (a) 0 min, (b) 30 mins, (c) 50 mins, (d) 90 mins, (e) 130 mins, and (f) 150 mins. The crack is highlighted by the yellow dotted line, and the crater formed by the spalling of material is highlighted by the green dotted box. Fe(Al, Cu) phase is highlighted by the red dotted box.

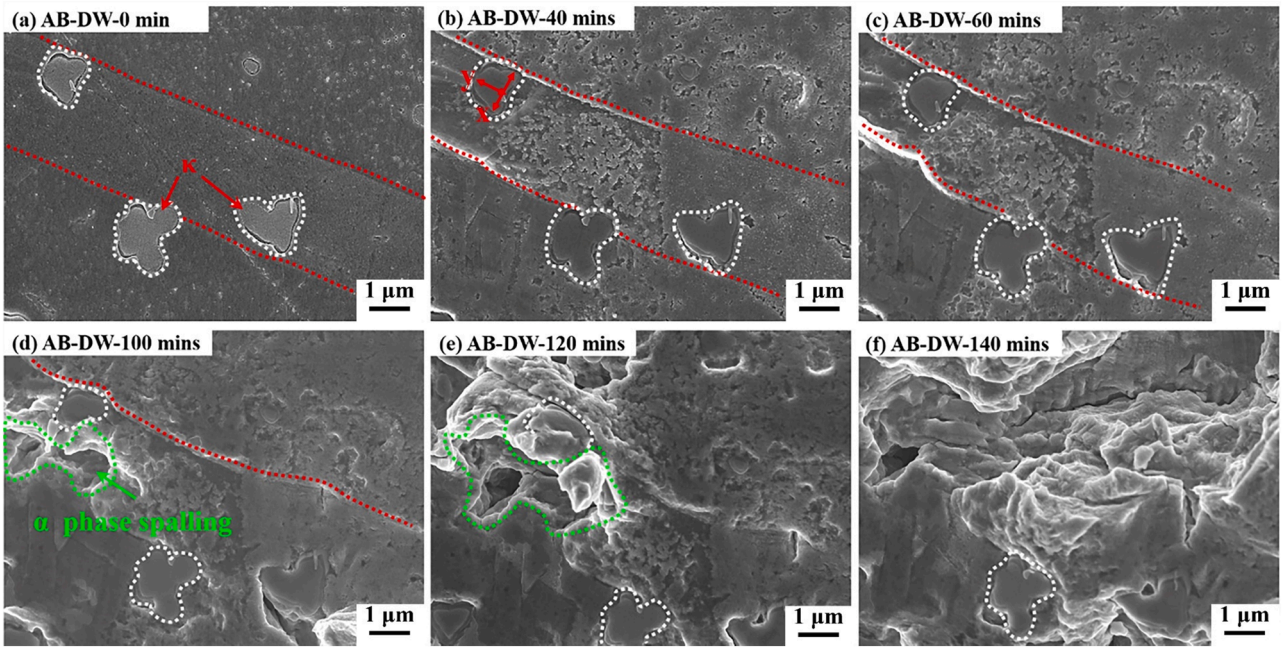

Fig. 8. The microstructural evolution of the AB at the α/κ interface during cavitation erosion in DW for (a) 0 min, (b) 30 mins, (c) 50 mins, (d) 90 mins, (e) 130 mins, and (f) 150 mins. The κ phase is highlighted by the white dotted box. The grain boundary is highlighted by the red dotted line, and the crater formed by the spalling of material is highlighted by the green dotted box.

means the α phase has better work hardening ability than the hard phases. After a short period of cavitation erosion, the α phase generates many dislocations in response to the action of microjets and shock waves [55]. However, these generated dislocations are unstable, and some dislocations are prone to slip during the subsequent cavitation erosion process [56]. These moving dislocations can be easily blocked by phase boundaries due to the high hardness of the hard phase, resulting in stress accumulation at the phase boundaries [29]. After more exposure to cavitation erosion, the accumulated stress causes severe deformation of the hard phase, and many cracks were also generated around the hard phase during the deformation process. After further exposure to cavitation erosion, the hard phase with the α phase can spall off from the sample surface, resulting in the formation of a cavitation crater. Forming a cavitation crater causes some of the accumulated stress to be released. However, the stress around the cavitation crater will accumulate again as the cavitation erosion time increases, which results in more mass loss and the formation of a larger cavitation crater [25]. Studies that worked with SEM observation on irons found the graphite-matrix interfaces and ferrite-austenite phase boundaries easily damaged at the early stage of cavitation erosion [57,58], which is similar to the results observed in

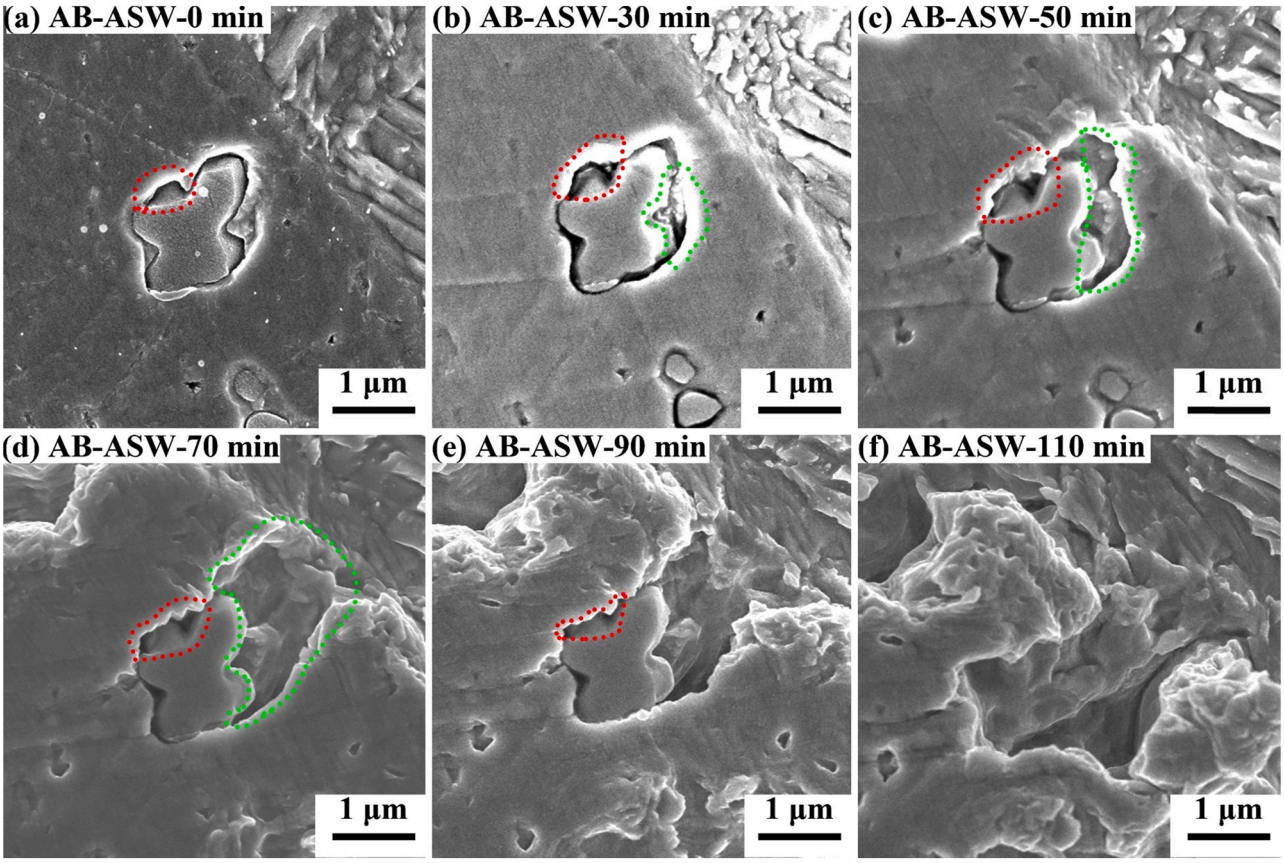

Fig. 9. The microstructural evolution of the AB at the α/κ interface during cavitation erosion in ASW solution for (a) 0 min, (b) 30 mins, (c) 50 mins, (d) 70 mins, (e) 90 mins, and (f) 110 mins. The craters formed by the spalling of material are highlighted by the green dotted box and the red dotted box.

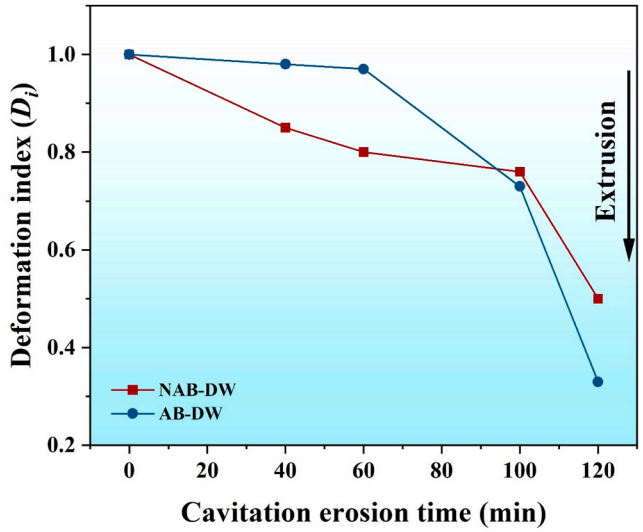

Fig. 10. Deformation index (D_i) of the NAB and AB under different test conditions. $D_i = (R_t^{xy}) / (R_0^{xy})$, where the R_t^{xy} is the length to width ratio of the κ phase at the t^{th} min. The x and y denote the length and width, which are marked in Figs. 4 and 8, respectively.

this study.

For the copper alloys immersed in ASW, the potential difference between different phases can be regarded as the driving force for selective phase corrosion [59,60]. The phase boundary atoms preferentially dissolved out due to their higher energy, which results in a series of reactions. Although the corrosion process of the copper alloys in ASW is complex, the current recognized process is the dissolution of aluminium and copper occurring at the phase boundary at first [61,62]:

$$Al + 4Cl^- \rightarrow AlCl_4^- + 3e^- \quad (1)$$

$$Cu + Cl^- \rightarrow CuCl + e^- \quad (2)$$

$$CuCl + Cl^- \rightarrow CuCl_2^- \quad (3)$$

As the $AlCl_4^-$, CuCl, and $CuCl_2^-$ are unstable, Al_2O_3 and Cu_2O are formed subsequently through the following reactions [63–65]:

$$2AlCl_4^- + 3H_2O \rightarrow Al_2O_3 + 6H^+ + 8Cl^- \quad (4)$$

$$2CuCl + H_2O \rightarrow Cu_2O + 2H^+ + 2Cl^- \quad (5)$$

$$2CuCl_2^- + H_2O \rightarrow Cu_2O + 4Cl^- + 2H^+ \quad (6)$$

Finally, the Cu_2O could be further oxidized to $Cu(OH)_2$ and $Cu_2(OH)_3Cl$, according to the following Eqs. (7) - (8):

$$Cu_2O + 3H_2O \rightarrow 2Cu(OH)_2 + 2H^+ + 2e^- \quad (7)$$

$$Cu_2O + Cl^- + 2H_2O \rightarrow Cu_2(OH)_3Cl + H^+ + 2e^- \quad (8)$$

As a result, a corrosion product film can be formed on the surface of the copper alloys, and the thickness can reach 900–1000 nm in a static corrosive environment [66]. The corrosion product film is composed of Al_2O_3 adjacent to the base metal and copper-containing corrosion products ($Cu(OH)_2$ and $Cu_2(OH)_3Cl$) in the outer regions [67]. However, it is difficult to form a complete passivation film on the surface of the copper alloys under cavitation erosion-corrosion conditions, which is attributed to the continuous destruction on the surface by cavitation erosion. Due to the rapid destruction of the passivation film, the

dissolution rate of the phase boundary atoms is much higher than that in a static condition, which results in the phase boundary of the hard phase being exposed entirely after a short period of cavitation erosion [68]. In addition, the dislocations generated during the cavitation erosion process can lead to the accumulation of stress on the surface of the samples, while the corrosive ASW can induce the release of the stress, which leads to the generation of cracks [25,69]. To illustrate the effect of crack generation in the α phase on the phase boundary stress accumulation process, critical deformation resistance of phase boundary (τ_{cp}) was introduced [14]:

$$\tau_{cp} = D * (\Delta\tau)^2 * (2\ G*b)^{-1} \quad (9)$$

D is the diameter of the α phase, G and b are the elastic modulus and Burgers vectors, which are constant values for a fixed lattice structure material. $\Delta\tau$ is the resolved shear stress of single dislocation, derived from the external force exerted by the cavitation microjets and shock waves. Assuming that the critical deformation resistance of the phase boundary (τ_{cp}) required to cause the deformation of the phase boundary is constant, great external input force ($\Delta\tau$) is required if the grain size (D) is small, meaning that the deformation of the phase boundary is more difficult in small-sized α phase. Due to the corrosive ASW inducing the release of stress, many cracks are generated [25], which is similar to the effect of D value reduction. Therefore, the higher the crack density in the α phase, the smaller the stress applied to the phase boundary, resulting in less deformation of the hard phase. In addition, the atoms in the phase boundary are continuously dissolved due to phase selective corrosion, which causes the cracks at the phase boundary to widen continuously with the extension of test time. The dissolution of the phase boundary causes the α phase and the hard phase to come out of contact, which means that the α phase needs to deform across the cracks before exerting force on the hard phase. The generation of many cracks and the dissolution of the phase boundary may partly explain the unobserved deformation of the hard phase during cavitation erosion in ASW.

3.5. Summary of the failure mechanisms

A schematic is shown in Fig. 11 demonstrating the failure mechanisms of copper alloys during the cavitation erosion process in DW and ASW. Before cavitation erosion in DW, no crack could be seen on the sample surface (Figs. 11**a**-1). After a short exposure to cavitation erosion, some dislocations were generated on the surface of the sample. As the cavitation erosion test continues, some dislocations would slip to the phase boundary, causing a slight deformation of the hard phase (Figs. 11**b**-1). After more exposure to cavitation erosion, more stress accumulated at phase boundaries, resulting in severe deformation of the hard phase and the generation of some cracks (Figs. 11**c**-1). Eventually,

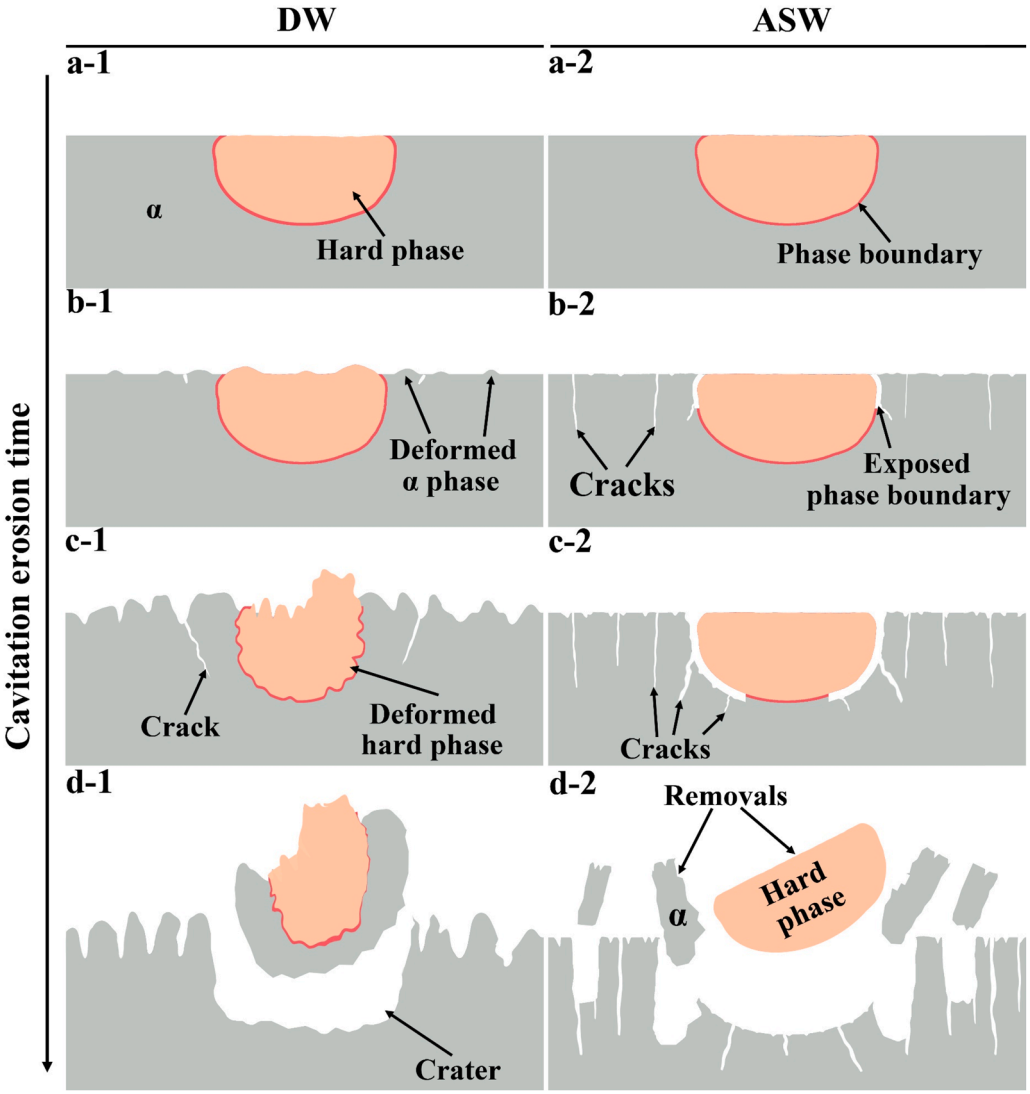

Fig. 11. Schematic diagrams showing the cavitation erosion failure mechanisms of the hard phase of copper alloys in DW (−1) and ASW (−2) solutions.

the continuous stress build-up led to the enlargement of the cracks around the hard phase, which eventually results in the exfoliation of the hard phase with some α phase and the generation of a cavitation crater (Figs. 11**d**-1). When the copper alloys were tested in ASW for a short time, the continued dissolution of the phase boundary caused partial exposure of the hard phase and cracks were observed due to the release of stress caused by the corrosive ASW. (Figs. 11**b**-2). As the cavitation erosion test continued, the cracks further increased, and the phase boundary was further dissolved (Figs. 11**c**-2). Eventually, the hard phase would be easily peeled off, forming a cavitation crater (Figs. 11**d**-2). Compared with the samples tested in DW, the hard phase on the surface of the samples tested in ASW was easier to peel off, and cracks were more likely to be generated. Since the hard phase plays the role of dispersion strengthening in copper alloys [32], it is obviously not conducive for copper alloys to resist cavitation erosion damage if the hard phases are peeled off easily. In addition, the cracks reduce the strength of the copper alloys, resulting in a reduced ability to resist cavitation erosion damage. At the same time, the crack is also an important nucleation site for cavitation, which makes the crack more vulnerable to cavitation microjet attack [70]. Therefore, the mass loss of copper alloys increases significantly undre cavitation erosion-corrosion conditions (Fig. 2).

4. Conclusions

This study investigated the cavitation erosion failure mechanisms of nickel aluminum bronze (NAB) and aluminum bronze (AB) in deionized water (DW) and artificial seawater (ASW) by SEM observation. It can be concluded as follows:

(1) At the early stage of cavitation erosion in DW, the hard phase could hinder the deformation of the α phase. This resulted in the local stress accumulation in the surrounding α phase, leading to the generation of cracks as the starting site of cavitation erosion.

(2) With the prolongation of cavitation erosion time in DW, the continuous accumulation of stress at the phase boundary caused severe deformation of the hard phase and the generation of many cracks in the surrounding α phase, which eventually led to the exfoliation of the second and some α phase.

(3) Phase selective corrosion could cause the dissolution of the phase boundary at the beginning of cavitation erosion in ASW, resulting in a decrease in the binding force between the hard phase and the α phase and making it easier to peel off.

(4) Corrosive ASW would induce the release of stress on the surface of the samples, which could lead to the generation of more cracks and the formation of more initial sites of cavitation erosion. As a result, the samples showed lower cavitation erosion resistance in ASW than that in DW.

(5) During the cavitation erosion test in ASW, no deformation of the hard phase was observed, which can be attributed to the continuous dissolution of the phase boundary and the release of stress due to the massive generation of cracks in the α phase.

(6) Improving the phase selective corrosion resistance of copper alloys may help enhance the cavitation erosion resistance in corrosive media.

Declaration of Competing Interest

The authors declare that they have no known competing financial interests or personal relationships that could have appeared to influence the work reported in this paper.

Acknowledgements

This work was supported by the Zhejiang Provincial Natural Science Foundation of China (grant # LZ22E090001), and Ningbo 3315 Talents Program (grant # 2020A-29-G).

Statement of originality

The authors assure that the contents of this contribution are original, and this paper has not been submitted to any other journal for publication, or not published before elsewhere, and this article contains no libelous or unlawful statements, and does not infringe on the rights of others.

References

[1] Sadeghi Omidreza, Bakhtiari-Nejad Marjan, Yazdandoost Fatemeh, Shahab Shima, Mirzaeifar Reza. Dissipation of cavitation-induced shock waves energy through phase transformation in NiTi alloys. Int J Mech Sci 2018;137:304–14. https://doi.org/10.1016/j.ijmecsci.2018.01.036.

[2] Lei Qiao, Yuping Wu, Sheng Hong, Jie Cheng. Ultrasonic cavitation erosion mechanism and mathematical model of HVOF sprayed Fe-based amorphous/nanocrystalline coatings. Ultrason Sonochem 2019;52:142–9. https://doi.org/10.1016/j.ultsonch.2018.11.010.

[3] Hardes C, Pöhl F, Röttger A, Thiele M, Theisen W, Esen C. Cavitation erosion resistance of 316L austenitic steel processed by selective laser melting (SLM. Addit Manuf 2019;29:100786. https://doi.org/10.1016/j.addma.2019.100786.

[4] Ye L, Zhu X, He Y, Wei X. Ultrasonic cavitation damage characteristics of materials and a prediction model of cavitation impact load based on size effect. Ultrason Sonochem 2020;66:105115. https://doi.org/10.1016/j.ultsonch.2020.105115.

[5] Caron Ronald N, Sharif Ahmed. Copper alloys: properties and applications. Reference Module in Materials Science and Materials Engineering. Elsevier; 2017.

[6] Melissaris Themistoklis, Schenke Sören, Bulten Norbert, van Terwisga Tom JC. Cavitation erosion risk assessment on a full-scale steerable thruster. Ocean Eng 2022;251:111019. https://doi.org/10.1016/j.oceaneng.2022.111019.

[7] Basumatary J, Wood RJK. Different methods of measuring synergy between cavitation erosion and corrosion for nickel aluminium bronze in 3.5% NaCl solution. Tribol Int 2020;147:104843. https://doi.org/10.1016/j.triboint.2017.08.006.

[8] Song QN, Xu N, Jiang X, Liu Y, Tong Y, Li JS, et al. Effect of sulfide concentration on the corrosion and cavitation erosion behavior of a manganese-aluminum bronze in 3.5% NaCl solution. J Mater Eng Perform 2019;28:4053–64. https://doi.org/10.1007/s11665-019-04150-8.

[9] Jayaprakash Arvind, Choi Jin-Keun, Chahine Georges L, Martin Farrel, Donnelly Martin, Franc Jean-Pierre , et al. Scaling study of cavitation pitting from cavitating jets and ultrasonic horns. Wear 2012;296:619–29. https://doi.org/10.1016/j.wear.2012.07.025.

[10] Yang Li, Ying Lian, Yanjun Sun. Cavitation erosion behavior of friction stir processed nickel aluminum bronze. J Alloy Compd 2019;795:233–40. https://doi.org/10.1016/j.jallcom.2019.04.302.

[11] Al Hashem A, Riad W. The role of microstructure of nickel-aluminium-bronze alloy on its cavitation corrosion behavior in natural seawater. Mater Charact 2002;48:37–41. https://doi.org/10.1016/S1044-5803(02)00196-1.

[12] Hanke Stefanie, Fischer Alfons, Beyer Matthias, Santos Jorge dos. Cavitation erosion of NiAl-bronze layers generated by friction surfacing. Wear 2011;273:32–7. https://doi.org/10.1016/j.wear.2011.06.002.

[13] Zhenbo Qin, Qi Zhang, Qin Luo, Zhong Wu, Bin Shen, Lei Liu, et al. Microstructure design to improve the corrosion and cavitation corrosion resistance of a nickel-aluminum bronze. Corros Sci 2018;139:255–66. https://doi.org/10.1016/j.corsci.2018.04.043.

[14] Zhang LM, Ma AL, Yu H, Umoh AJ, Zheng YG. Correlation of microstructure with cavitation erosion behaviour of a nickel-aluminum bronze in simulated seawater. Tribol Int 2019;136:250–8. https://doi.org/10.1016/j.triboint.2019.03.071.

[15] Basumatary J, Wood RJK. Synergistic effects of cavitation erosion and corrosion for nickel aluminium bronze with oxide film in 3.5% NaCl solution. Wear, 376- 2017;377:1286–97. https://doi.org/10.1016/j.wear.2017.01.047.

[16] Tang CH, Cheng FT, Man HC. Improvement in cavitation erosion resistance of a copper-based propeller alloy by laser surface melting. Surf Coat Technol 2004;182:300–7. https://doi.org/10.1016/j.surfcoat.2003.08.048.

[17] Yang Li, Ying Lian, Yanjun Sun. Comparison of cavitation erosion behaviors between the as-cast and friction stir processed Ni-Al bronze in distilled water and artificial seawater. J Mater Res Technol 2021;13:906–18. https://doi.org/10.1016/j.jmrt.2021.05.015.

[18] Cottam R, Luzin V, Moody H, Edwards D, Majumdar A, Wong YC, et al. The role of microstructural characteristics in the cavitation erosion behaviour of laser melted and laser processed nickel-aluminium bronze. Wear 2014;317:56–63. https://doi.org/10.1016/j.wear.2014.05.002.

[19] Yongan Sun, Haibo Wang, Wei Liu, Guolin Song, Qiulin Li. Improvement of surface resistance to cavitation corrosion of nickel aluminum bronze by electropulsing-assisted ultrasonic surface rolling process. Surf Coat Technol 2019;368:215–23. https://doi.org/10.1016/j.surfcoat.2019.03.045.

[20] Ryl J, Darowicki K, Slepski P. Evaluation of cavitation erosion-corrosion degradation of mild steel by means of dynamic impedance spectroscopy in galvanostatic mode. Corros Sci 2011;53:1873–9. https://doi.org/10.1016/j.corsci.2011.02.004.

[21] Tang CH, Cheng FT, Man HC. Effect of laser surface melting on the corrosion and cavitation erosion behaviors of a manganese-nickel-aluminium bronze. Mater Sci Eng, A 2004;373:195–203. https://doi.org/10.1016/j.msea.2004.01.016.

[22] Luo Qin, Zhang Qi, Qin Zhenbo, Wu Zhong, Shen Bin, Liu Lei, et al. The synergistic effect of cavitation erosion and corrosion of nickel-aluminum copper surface layer on nickel-aluminum bronze alloy. J Alloy Compd 2018;747:861–8. https://doi.org/10.1016/j.jallcom.2018.03.103.

[23] Ye Tian Rui Yang, Zhoupeng Gu Hang Zhao, Xianqian Wu Shahed Taghian Dehaghani, Chen Hao, Liu Xiaomei, Xiao Tonghu, et al. Ultrahigh cavitation erosion resistant metal-matrix composites with biomimetic hierarchical structure. Compos Part B-Eng 2022;234:109730. https://doi.org/10.1016/j.compositesb.2022.109730.

[24] Yang Li, Ying Lian, Yanjun Sun. Synergistic effect between cavitation erosion and corrosion for friction stir processed NiAl Bronze in artificial seawater. Met Mater Int 2021;27:5082–94. https://doi.org/10.1007/s12540-020-00916-1.

[25] Ye Tian, Hang Zhao, Rui Yang, Xiaomei Liu, Xiuyong Chen, Jiahao Qin, et al. *In-situ* SEM investigation on stress-induced microstructure evolution of austenitic stainless steels subjected to cavitation erosion and cavitation erosion-corrosion. Mater Des 2022;213:110314. https://doi.org/10.1016/j.matdes.2021.110314.

[26] Zhenhua Wang, Bing Zhang. *In-situ* study on cavitation erosion behavior of super ferritic stainless steel. Wear 2021;482–483:203986. https://doi.org/10.1016/j.wear.2021.203986.

[27] Rui Yang, Ye Tian, Nengliang Huang, Pengfei Lu, Hao Chen, Hua Li, et al. Effects of CeO_2 addition on microstructure and cavitation erosion resistance of laser-processed Ni-WC composites. Mater Lett 2022;311:131583. https://doi.org/10.1016/j.matlet.2021.131583.

[28] Ni DR, Xiao BL, Ma ZY, Qiao YX, Zheng YG. Corrosion properties of friction–stir processed cast NiAl bronze. Corros Sci 2010;52:1610–7. https://doi.org/10.1016/j.corsci.2010.02.026.

[29] Ki Han Kim, Georges Chahine, Jean Pierre Franc, Karimi Ayat. Advanced experimental and numerical techniques for cavitation erosion prediction. Springer,; 2014.

[30] Haijun Zhang, Yongfeng Gong, Xiuyong Chen, André McDonald, Li Hua. A comparative study of cavitation erosion resistance of several HVOF-sprayed coatings in deionized water and artificial seawater. J Therm Spray Technol 2019;28:1060–71. https://doi.org/10.1007/s11666-019-00869-x.

[31] D1141–98(2013), Standard practice for the preparation of substitute ocean water, ASTM International, West Conshohocken, PA, 2013.

[32] Anantapong J, Uthaisangsuk V, Suranuntchai S, Manonukul A. Effect of hot working on microstructure evolution of as-cast nickel aluminum bronze alloy. Mater Des 2014;60:233–43. https://doi.org/10.1016/j.matdes.2014.03.033.

[33] Orzolek Sean M, Semple Jennifer K, Fisher Charles R. Influence of processing on the microstructure of nickel aluminum bronze (NAB. Addit Manuf 2022;56:102859. https://doi.org/10.1016/j.addma.2022.102859.

[34] Shuiyuan Yang, Yu Su, Cuiping Wang, Xingjun Liu. Microstructure and properties of Cu-Al-Fe high-temperature shape memory alloys. Mater Sci Eng, B 2014;185:67–73. https://doi.org/10.1016/j.mseb.2014.02.001.

[35] Mustafa Yaşar, Yahya Altunpak. The effect of aging heat treatment on the sliding wear behaviour of Cu-Al-Fe alloys. Mater Des 2009;30:878–84. https://doi.org/10.1016/j.matdes.2008.05.041.

[36] Huttunen Saarivirta E, Isotahdon E, Metsäjoki J, Salminen T, Carpén L, Ronkainen H. Tribocorrosion behaviour of aluminium bronze in 3.5 wt% NaCl solution. Corros Sci 2018;144:207–23. https://doi.org/10.1016/j.corsci.2018.08.058.

[37] Sheng Li Jiang, Yu Gui Zheng, Zhi Ming Yao. Cavitation erosion behaviour of 20SiMn low alloy steel in Na_2SO_4 and $NaHCO_3$ solutions. Corros Sci 2006;48:2614–32. https://doi.org/10.1016/j.corsci.2005.09.004.

[38] Zhibin Zheng Jun Long, Shuai Wang Hui Li, Juan Wang Kaihong Zheng. Cavitation erosion-corrosion behaviour of Fe-10Cr martensitic steel microalloyed with Zr in 3.5% NaCl solution. Corros Sci 2021;184:109382. https://doi.org/10.1016/j.corsci.2021.109382.

[39] ASTM G32–10, Standard test method for cavitation erosion using vibratory apparatus, ASTM International, West Conshohocken, PA, 2010.

[40] Zhengliang Liu Azim Khan, Mingli Shen Shenglong Zhu, Chaoliu Zeng Fuhui Wang, Fu Chao. Microstructure and cavitation erosion resistance of arc ion plating NiCrAlY coating on the 304L stainless steel. Tribol Int 2022;173:107618. https://doi.org/10.1016/j.triboint.2022.107618.

[41] Renshi Zheng Xiaoyu Zhao, Leilei Dong Gang Liu, Yi Huang Yunze Xu. On the cavitation erosion-corrosion of pipeline steel at different locations of Venturi pipe. Eng Fail Anal 2022;138:106333. https://doi.org/10.1016/j.engfailanal.2022.106333.

[42] Yang Ding Yuting Lv, Kai Chen Bingjie Zhao, Yuanfei Han Liqiang Wang, Lu Weijie. Effects of microstructure on the stress corrosion cracking behavior of nickel-aluminum bronze alloy in 3.5% NaCl solution. Mater Sci Eng, A 2018;733:361–73. https://doi.org/10.1016/j.msea.2018.07.066.

[43] Chengxi Wang Chuanhai Jiang, Ming Chen Lianbo Wang, Huabing Liu Vincent Ji. Residual stress and microstructure evolution of shot peened Ni-Al bronze at elevated temperatures. Mater Sci Eng, A 2017;707:629–35. https://doi.org/10.1016/j.msea.2017.09.098.

[44] Karimi A, Martin JL. Cavitation erosion of materials. Int Mater Rev 1986;31:1–26. https://doi.org/10.1179/imtr.1986.31.1.1.

[45] Guiyan Gao Zheng Zhang. Cavitation erosion mechanism of 2Cr13 stainless steel. Wear, 488- 2022;489:204137. https://doi.org/10.1016/j.wear.2021.204137.

[46] Osman Asi. Failure of a diesel engine injector nozzle by cavitation damage. Eng Fail Anal 2006;13:1126–33. https://doi.org/10.1016/j.engfailanal.2005.07.021.

[47] Hidehiro Yoshida Kenji Yokoyama, Naoya Shibata Yuichi Ikuhara, Sakuma Taketo. High-temperature grain boundary sliding behavior and grain boundary energy in cubic zirconia bicrystals. Acta Mater 2004;52:2349–57. https://doi.org/10.1016/j.actamat.2004.01.026.

[48] Tadao Watanabe. Grain boundary sliding and stress concentration during creep. Metall Trans A 1983;14:531–45. https://doi.org/10.1007/BF02643771.

[49] Mori G, Scherer D, Schwentenwein S, Warbichler P. Intergranular stress corrosion cracking of copper in nitrite solutions. Corros Sci 2005;47:2099–124. https://doi.org/10.1016/j.corsci.2004.09.024.

[50] Beibei Zhang, Jianzhang Wang, Fengyuan Yan. Load-dependent tribocorrosion behaviour of nickel-aluminium bronze in artificial seawater. Corros Sci 2018;131:252–63. https://doi.org/10.1016/j.corsci.2017.11.028.

[51] Kosky Philip, Balmer Robert, Keat William, Wise George. Chapter 13 - Materials Engineering. In: Kosky P, Balmer R, Keat W, Wise G, editors. Exploring Engineering (Fifth Edition). Academic Press; 2021. p. 293–315.

[52] Michael Zaiser, Alfred Seeger. Chapter 56 Long-range internal stresses, dislocation patterning and work-hardening in crystal plasticity. In: Nabarro FRN, Duesbery MS, editors. Dislocations in Solids. Elsevier; 2002. p. 1–100.

[53] Al Hashem A, Caceres PG, Riad WT, Shalaby HM. Cavitation corrosion behavior of cast nickel-aluminum bronze in seawater. Corrosion 1995;51:331–42. https://doi.org/10.5006/1.3293598.

[54] Cameron Barr, Pateras Aaron, Molotnikov Andrey, Clarke David, Brandt Milan. Effect of composition on the tensile and corrosion performance of nickel aluminium bronze produced via laser powder bed fusion. Addit Manuf 2022;54:102771. https://doi.org/10.1016/j.addma.2022.102771.

[55] Karimi A, Maamouri M, Martin JL. Cavitation-erosion-induced microstructures in copper single crystals. Mater Sci Eng, A 1989;113:287–96. https://doi.org/10.1016/0921-5093(89)90317-1.

[56] Krystyna Krella Alicja. Degradation of AlMg2 aluminium alloy caused by cavitation - An effect of cavitation intensity. Mater Charact 2017;130:219–29. https://doi.org/10.1016/j.matchar.2017.06.015.

[57] Abreu Marcio, Sundberg Jill, Elfsberg Jessica, Jonsson Stefan. Morphology and mechanisms of cavitation damage on lamellar gray iron surfaces. Wear 2020;456–457:203324. https://doi.org/10.1016/j.wear.2020.203324.

[58] Abreu Marcio, Elfsberg Jessica, Jonsson Stefan. Cavitation erosion behavior of austempered ductile irons of increasing hardness. Wear 2021;484–485:204036. https://doi.org/10.1016/j.wear.2021.204036.

[59] Song QN, Zheng YG, Ni DR, Ma ZY. Studies of the nobility of phases using scanning Kelvin probe microscopy and its relationship to corrosion behaviour of Ni-Al bronze in chloride media. Corros Sci 2015;92:95–103. https://doi.org/10.1016/j.corsci.2014.11.039.

[60] Luo Qin, Qin Zhenbo, Wu Zhong, Shen Bin, Liu Lei, Hu Wenbin. The corrosion behavior of Ni-Cu gradient layer on the nickel aluminum-bronze (NAB) alloy. Corros Sci 2018;138:8–19. https://doi.org/10.1016/j.corsci.2018.03.050.

[61] Qin Zhenbo, Xia Dahai, Zhang Yiwen, Wu Zhong, Liu Lei, Lv Yuting, et al. Microstructure modification and improving corrosion resistance of laser surface quenched nickel-aluminum bronze alloy. Corros Sci 2020;174:108744. https://doi.org/10.1016/j.corsci.2020.108744.

[62] Song QN, Zheng YG, Ni DR, Ma ZY. Characterization of the corrosion product films formed on the as-cast and friction-stir processed Ni-Al bronze in a 3.5 wt% NaCl solution, Corrosion 2015;71:606–14. https://doi.org/10.5006/1391.

[63] Campbell SA, Radford GJW, Tuck CDS, Barker BD. Corrosion and galvanic compatibility studies of a high-strength copper-nickel alloy. Corrosion 2002;58:57–71. https://doi.org/10.5006/1.3277305.

[64] Metikoš Huković M, Babić R, Škugor Rončević I, Grubač Z. Corrosion behavior of the filmed copper surface in saline water under static and jet impingement conditions. 025002-025001-025002-025008 Corrosion 2012;68. https://doi.org/10.5006/1.3683224.

[65] Ma AL, Jiang SL, Zheng YG, Ke W. Corrosion product film formed on the 90/10 copper-nickel tube in natural seawater: Composition/structure and formation mechanism. Corros Sci 2015;91:245–61. https://doi.org/10.1016/j.corsci.2014.11.028.

[66] Wharton JA, Stokes KR. The influence of nickel-aluminium bronze microstructure and crevice solution on the initiation of crevice corrosion. Electrochim Acta 2008;53:2463–73. https://doi.org/10.1016/j.electacta.2007.10.047.

[67] Schüssler A, Exner HE. The corrosion of nickel-aluminium bronzes in seawater-I. Protective layer formation and the passivation mechanism. Corros Sci 1993;34:1793–802. https://doi.org/10.1016/0010-938X(93)90017-B.

[68] Tian Ye, Zhao Hang, Yang Rui, Liu Xiaomei, Li Hua, Chen Xiuyong. Effects of *Bacillus sp*. adhesion on cavitation erosion behaviour of nickel aluminium bronze in artificial seawater. Wear 2022;498–499:204344. https://doi.org/10.1016/j.wear.2022.204344.

[69] Lynch SP. 1 - Mechanistic and fractographic aspects of stress-corrosion cracking (SCC). In: Raja VS, Shoji T, editors. Stress Corrosion Cracking. Woodhead Publishing; 2011. p. 3–89.

[70] Singh Navneet K, Vinay Gidla, Ang Andrew SM, Mahajan Dhiraj K, Singh Harpreet. Cavitation erosion mechanisms of HVOF-sprayed Ni-based cermet coatings in 3.5% NaCl environment. Surf Coat Technol 2022;434:128194. https://doi.org/10.1016/j.surfcoat.2022.128194.